Volume 19
Number 32
28 August 2023
Pages 6059–6186

Soft Matter

rsc.li/soft-matter-journal

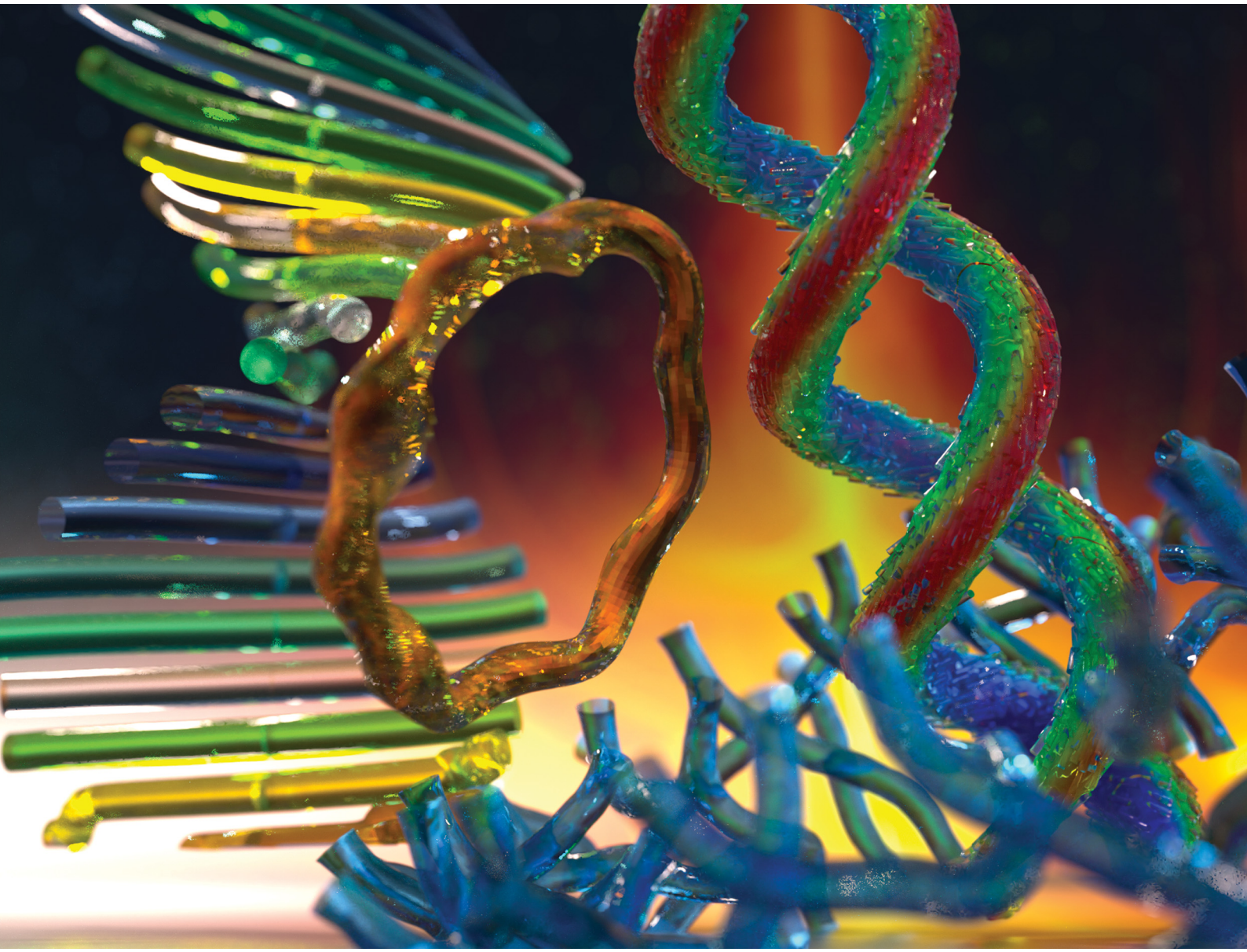

ISSN 1744-6848

ROYAL SOCIETY OF CHEMISTRY

PAPER
Juan P. Hernández-Ortiz, Juan J. de Pablo *et al.*
Curvature and confinement effects on chiral liquid crystal morphologies

Soft Matter

PAPER

View Article Online
View Journal | View Issue

Check for updates

Cite this: *Soft Matter*, 2023, **19**, 6066

Curvature and confinement effects on chiral liquid crystal morphologies

Viviana Palacio-Betancur, [a] Julio C. Armas-Pérez, [b] Juan P. Hernández-Ortiz *[acd] and Juan J. de Pablo *[ae]

Received 31st March 2023,
Accepted 31st May 2023

DOI: 10.1039/d3sm00437f

rsc.li/soft-matter-journal

Chiral liquid crystals (ChLCs) exhibit an inherent twist that originates at the molecular scale and can extend over multiple length scales when unconstrained. Under confinement, the twist is thwarted, leading to formation of defects in the molecular order that offer distinct optical responses and opportunities for colloidal driven assembly. Past studies have explored spheroidal confinement down to the nanoscopic regime, where curved boundaries produce surface defects to accommodate topological constraints and restrict the propagation of cuboidal defect networks. Similarly, strict confinement in channels and shells has been shown to give rise to escaped configurations and skyrmions. However, little is known about the role of extrinsic curvature in the development of cholesteric textures and Blue Phases (BP). In this paper, we examine the palette of morphologies that arises when ChLCs are confined in toroidal and cylindrical cavities. The equilibrium morphologies are obtained following an annealing strategy of a Landau-de Gennes free energy functional. Three dimensionless groups are identified to build phase diagrams: the natural twist, the ratio of elastic energies, and the circumscription of a BP cell. Curvature is shown to introduce helical features that are first observed as a Double Twist, and progress to Chiral Ribbons and, ultimately, Helical BP and BP. Chiral ribbons are examined as useful candidates for driven assembly given their tunability and robustness.

Open Access Article. Published on 08 June 2023. Downloaded on 4/3/2026 6:47:20 PM.
This article is licensed under a Creative Commons Attribution 3.0 Unported Licence.

1 Introduction

The role of curvature on the ordering and assembly of building blocks is fundamental to the understanding of flexible bilayer membranes,[1,2] viral capsids,[3–5] spherical crystallography,[6] quasi-2D materials,[7,8] and active matter.[9,10] From a 2D perspective, curvature provides subtle changes to the local order, leading to bistability and a means to manipulate the preferred alignment through the confining geometry.[8,11,12] In three dimensions, confinement provides an additional parameter with which to balance bulk elasticity and surface curvature for design of responsive materials.[13–18] In the context of liquid crystals, orientational order becomes frustrated and defects, regions of low order, emerge as a result of topological constraints.[15,19–22]

Past studies have produced stable LC morphologies through geometrical confinement, particularly for chiral liquid crystals (ChLCs) where elongated molecules collectively break rotational symmetry and organize along a main helical path, thereby favoring twist over splay or bending deformations. In spherical cavities, ChLCs' inherent twist conforms to the surface curvature and generate frustrated concentric structures such as the Twisted Bipolar and the Radial Spherical Structure.[21–27] Highly chiral ChLCs contain disclination lines in the bulk, and curvature can mold them into hybrid structures.[27–30] For shells, the inner anchoring conditions generate escaped configurations, and the shell homogeneity and thickness become important parameters to control morphology.[31–38] More intricate geometries, such as droplets with handles, have been found to guide disclination lines into knots and other non-trivial textures.[39–42]

Toroidal and cylindrical confinement offer ample grounds for discovery of new phases, as demonstrated in experiments where the ground state of a non-chiral LC is the double twisted morphology,[39,43–46] in contrast to the uniform orientation along the main axis of a cylindrical cavity.[47–49] Under homeotropic confinement, LCs have been shown to exhibit spontaneous twist resulting in escaped radial configurations induced by the curved boundaries.[50,51] From a computational standpoint, traditional numerical methods are generally limited by the need to

[a] *Pritzker School of Molecular Engineering, University of Chicago, Chicago, IL 60637, USA. E-mail: depablo@uchicago.edu*
[b] *División de Ciencias e Ingenierías, Campus León, Universidad de Guanajuato, Loma del Bosque 103, León (Gto.) 37150, Mexico*
[c] *Departamento de Materiales y Minerales, Universidad Nacional de Colombia—Sede Medellín, Medellín, Colombia. E-mail: jphernandezo@unal.edu.co*
[d] *Colombia/Wisconsin One-Health Consortium, Universidad Nacional de Colombia Sede Medellín, Medellín, Colombia*
[e] *Materials Science Division, Argonne National Laboratory, Lemont, IL 60439, USA*

This journal is © The Royal Society of Chemistry 2023

Open Access Article. Published on 08 June 2023. Downloaded on 4/3/2026 6:47:20 PM.
This article is licensed under a Creative Commons Attribution 3.0 Unported Licence.

formulate an ansatz (or "initial guess") corresponding to each geometry,[45,52] and by the scale of the discretization needed to capture a morphology's nuances.[53]

ChLCs offer several characteristics of interest for photonic and electro-optical devices. They exhibit fast response times and rich optical behaviors. The characteristic length scale of the helical trajectory, or molecular pitch, determine the equilibrium morphology of the system. For long pitches, the material exhibits a cholesteric phase, where molecules can twist uniformly without forming defects. For a sufficiently short pitch, defect lines form spontaneously and self-organize into space filling lattices with cubic symmetry, leading to the so-called Blues Phases (BPs).[54]

However versatile, BPs are only stable over a narrow range of temperature. Furthermore, in the bulk they form polycrystalline domains, posing challenges to applications.[55,56] External stimuli can help enhance and stabilize morphologies of interest. Lithographic patterns, for example, have been successful in achieving monocrystalline domains of BPII and BPI, where the substrate chemistry is tailored to guide the orientation of the BP unit cells.[57,58] Polymerization has also been used to enhance the thermal stability of BPs, by setting the underlying defect network into a permanent scaffold.[59–62]

More recently, Negro *et al.* reported a detailed analysis of the patterns that appear on the surface of chiral LC shells. These authors relied on lattice Boltzmann simulations to identify the equilibrium morphologies of highly chiral LCs as they transition into an ordered phase from an isotropic state.[63] Building on that work, in this study we examine how geometrical frustration in toroidal and cylindrical cavities can be manipulated to preserve key characteristics of chiral nematics while introducing new geometrical features that do not arise when in bulk. Specifically, curvature is used to engineer new mesophases of ChLCs – curvature couples to defects by screening their topological charge. Recent theoretical reports indicate that strict planar confinement of 2D ChLCs hinders the development of double twist, leading to the formation of a novel chiral structure.[64]

In Section 2 we outline the details of the phenomenological model adopted here, as well as the numerical methods used to find equilibrium configurations. Section 3 introduces our results and discussion by presenting the underlying free energy surface as a function of chirality and cavity size. We continue by presenting phase diagrams at different temperatures, and a more detailed analysis of the surface patterns corresponding to each system. In Section 4 we provide a short summary of our findings and several remarks about future applications of this work.

2 Models and methods

The free energy functional includes a short-range Landau polynomial expansion in $\mathbf{Q}(\mathbf{x})$ to model the isotropic-nematic transition, a long-range functional that accounts for elastic distortions, and a surface contribution that imposes a preferred orientation at the boundaries.

$$\begin{aligned} F(\mathrm{Q}) &= \int \mathrm{d}^3\mathrm{x}\left[\frac{A}{2}\left(1-\frac{U}{3}\right)\mathrm{tr}(\mathrm{Q}^2) - \frac{AU}{3}\mathrm{tr}(\mathrm{Q}^3) + \frac{AU}{4}\mathrm{tr}(\mathrm{Q}^2)^2\right. \\ &\quad \left. + \frac{L_1}{2}\frac{\partial Q_{ij}}{\partial x_k}\frac{\partial Q_{ij}}{\partial x_k} + \frac{L_5}{2}\varepsilon_{ikl}Q_{ij}\frac{\partial Q_{lj}}{\partial x_k}\right] \\ &\quad + \oint \mathrm{d}^2\mathrm{x}\left[\frac{W}{2}\left(\bar{\mathbf{Q}}-\bar{\mathbf{Q}}_\perp\right)^2 + \frac{W}{4}\left(\bar{\mathbf{Q}}:\bar{\mathbf{Q}}-S^2\right)^2\right]. \end{aligned} \tag{1}$$

The model parameters include the Landau coefficient A that sets the energy density scale, the dimensionless parameter U that determines the IN transition (inverse temperature); L_1 and L_5 are the elastic constants and W represents the strength of the surface anchoring. Additionally, the preferred orientation at the boundaries is tangential and is determined by the planar projection of $\mathbf{Q}$ as $\bar{\mathbf{Q}}_\perp = \mathbf{p}\cdot\bar{\mathbf{Q}}\cdot\mathbf{p}$ with $\bar{\mathbf{Q}} = \mathbf{Q} + S\boldsymbol{\delta}/3$ and $\mathbf{p} = \boldsymbol{\delta} - \boldsymbol{\nu}\boldsymbol{\nu}$. Details of the free energy densities in eqn (1) can be found in our previous works.[27,65–67]

Two characteristic length scales arise naturally from the free energy functional: the nematic coherence length $\xi_\mathrm{N} = \sqrt{L_1/A}$, and the surface extrapolation length $\xi_\mathrm{S} = L_1/W$. The elastic constants L_i are related to the different elastic moduli and chirality. For a uniaxial LC under a one-elastic constant approximation, they can be estimated through $L_1 = k_{11}/2S^2$ and $L_5 = 2q_0k_{22}/S^2$. L_5 quantifies the chirality of the LC with inverse pitch, $q_0 = 1/p_0$.

For efficient exploration of configuration space, we adopt a theoretically-informed Monte Carlo relaxation introduced in our previous works.[27,65–67] This approach is particularly effective for discovery of unknown morphologies, particularly in systems with a rough free energy surface. The minimization is achieved by performing random changes to the $\mathbf{Q}$ tensor according to a Metropolis algorithm to sample different morphologies of the free energy functional outlined above. The uniform sampling over the five independent components of $\mathbf{Q}$ is ensured by mapping the tensor onto an orthonormal basis introduced by Hess *et al.*[68] This replaces all tensor operations by faster, scalar ones.

Trial moves are accepted with probability $P_\mathrm{acc}(o \to n) = \min[1, \exp(-\beta\Delta F)]$, where $\beta^{-1} = k_\mathrm{B}\hat{T}$, k_B is the Boltzmann constant, $\hat{T}$ is an artificial temperature and ΔF is the change in the free energy due to changes in $\mathbf{Q}$. The domains are discretized into quadratic tetrahedral elements in Cubit (ver 14.1)[69] and optimized with the libMesh library.[70] The numerical integration to calculate the free energy is implemented with a Gauss–Legendre quadrature over the elements. The finite element-based meshing allows us to capture fine details of the geometry while providing a robust framework for non-linear behavior,[26,27,30,71] and is able to find equilibrium configurations consistent with those obtained by more traditional minimization techniques.[65–67]

The toroidal and cylindrical cavities shown in Fig. 1 ($R = 500$ nm and $r_0 \in [100, 250]$ nm) impose planar degenerate alignment with moderate ($W = 1 \times 10^{-4}$ J m^{-2}) to weak ($W = 1 \times 10^{-6}$ J m^{-2})

Open Access Article. Published on 08 June 2023. Downloaded on 4/3/2026 6:47:20 PM.
This article is licensed under a Creative Commons Attribution 3.0 Unported Licence.

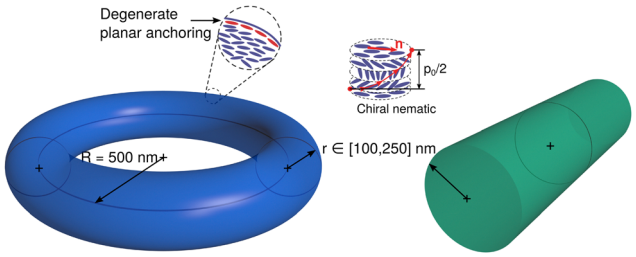

Fig. 1 Schematic representation of the toroidal and cylindrical cavities used to confine the chiral liquid crystal. The major radius of the toroid is R = 500 nm, while the radius of the cylinder r_0 varies between 100–250 nm. Surfaces impose degenerate planar anchoring alignment of the chiral material.

anchoring strength onto a chiral liquid crystal with pitch $p_o \in [100, 1000]$ nm. The nematic parameter is close to the IN transition, between $U = 2.7$ and $U = 2.9$, the regime in which BPs are stable in the bulk. The parameters for 4′-pentyl-4-cyanobiphenyl (5CB) are used as the model system with $A = 1 \times 10^5$ J m^{-3}, $L_1 = 5.11$ pN, and $\xi_N = 7.15$ nm. The free energy minimization requires approximately 4×10^5 Monte Carlo cycles. The system was quenched over five stages through $\hat{T}$. The meshes for these simulations vary in size according to the confinement size r_0; on average, they are comprised of 3×10^5 nodes and 2×10^5 elements for $r_0 = 100$ nm, and up to 9.5×10^5 nodes and 7×10^5 elements for $r_0 = 250$ nm.

3 Results

We begin our discussion by exploring the free energy contributions as a function of chirality and confinement, shown in Fig. 2a. For convenience, we use the dimensionless group $2q_0r_0$, analog to the chirality, which characterizes the natural twist in the confined system and allows us to collapse our results onto master curves shown in gray.

At low chirality, in the cholesteric (Chol) regime, all components of the free energy are close to zero, meaning that at equilibrium the resulting configuration is uniform and without defects, and the orientation of the LC at the boundary follows its curvature. For higher chirality, the material adopts a double twist configuration that results in a cuboidal defect network (Blue Phases, BP). Their emergence increases the Landau-de Gennes free energy, and the confluence of double twist domains creates regions of high splay, as reflected by the corresponding elastic contribution. At the boundary, the curvature interrupts the cubic symmetry of the defect network and produces a fingerprint pattern, a collection of half-skyrmions that will be described later in our analysis.

The ratio between chiral and splay elastic contributions serves as a proxy for the family of morphologies that arise in these systems, illustrated in Fig. 2b as a function of natural twist. Two lines serve to delineate the characteristics of the morphologies at equilibrium. The first is $|F_{Ch}|/F_{Splay} = 2$, and refers to the limiting energy for disclination lines to interweave the bulk of the system. The second line is defined by the

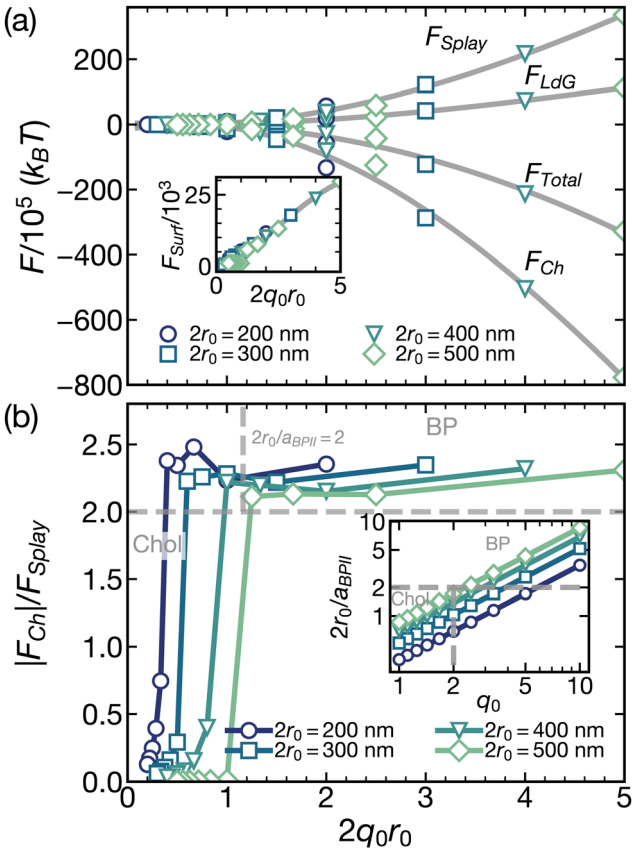

Fig. 2 (a) Free energy contributions as a function of chirality parameter q_0 scaled by torus inner radius r_0. Markers indicate the radius for the toroidal cavity. The inset shows the surface free energy contribution. Gray curves are polynomial fits of each free energy contribution. (b) Ratio of chiral and splay elastic energies as a function of chirality q_0 scaled by cavity radius r_0. The inset shows the ratio between cavity radius and unit cell size for Blue Phase II a_{BPII} as chirality q_0 increases.

balance between the cavity size ($2r_0$) and the Blue Phase unit cell a_{BP}, and plays a crucial role in systems with high chirality. For $2r_0/a_{BP} < 2$, confinement frustrates a fully developed BP cell, and the disclination lines adopt helical features conforming to the geometry. In this case, since $U = 2.7$, the unit cell is that of the Blue Phase II calculated as $a_{BPII} = p_0/1.72$. The inset in Fig. 2b shows the ratio $2r_0/a_{BPII}$ as a function of inverse pitch q_0, where a horizontal line delimits the systems in which helical morphologies are favored over fully developed Blue Phases.

The free energy analysis is consistent with the phase diagrams generated in terms of $q_0 = 1/p_0$ and $2r_0$, shown in Fig. 3 for (a) $U = 2.7$ and (b) $U = 2.9$ in a toroidal cavity. Highlighted markers in the phase diagram correspond to the morphologies illustrated in Fig. 3c. The first three morphologies occur at low chirality: Double Twist (DT), Twisted Ribbon (TR), and Helical Ribbon (HR). They are best described by the alignment of the director with respect to the major (toroidal) axis. First, the DT is a cholesteric morphology and exhibits a continuous twist in the radial direction. At the core of the cavity, the director is aligned with the toroidal axis such that the midline is straight. At the boundary, the director is tangential to the surface and is tilted

 This journal is © The Royal Society of Chemistry 2023

Open Access Article. Published on 08 June 2023. Downloaded on 4/3/2026 6:47:20 PM.
This article is licensed under a Creative Commons Attribution 3.0 Unported Licence.

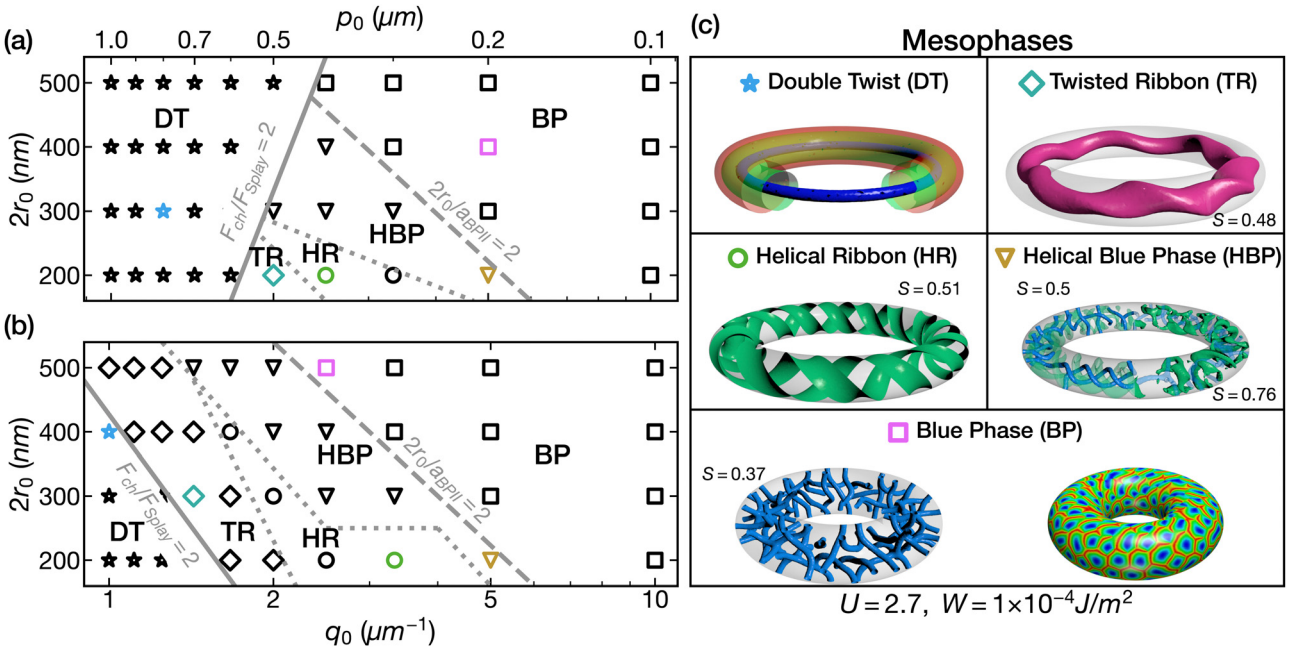

Fig. 3 Phase diagram and mesophases of a chiral liquid crystal with pitch $p_0 = 1/q_0$ confined in a toroidal cavity of diameter $2r_0$ under moderate planar anchoring ($W = 1 \times 10^{-4}$ J m^{-2}) at (a) $U = 2.7$ and (b) $U = 2.9$. (c) Morphologies corresponding to the highlighted markers in the phase diagrams: Double Twist (DT), Twisted Ribbon (TR), Helical Ribbon (HR), Helical Blue Phase (HBP), Blue Phase (BP).

with respect to the toroidal axis. The illustration in Fig. 3c shows three concentric tubes, each corresponding to regions in which the director tilt with respect to the midline is 0° (blue), 20° (green) and 45° (red).

As chirality increases, a smooth double twist within the torus can no longer be sustained, and each concentric layer of the DT buckles to form a twisted ribbon (TR). Each ribbon retains a straight midline while isosurfaces of the order parameter exhibit saddle-like curvature, as illustrated by the magenta ribbon with $S = 0.48$ in Fig. 3c. Additional twisting of the order field requires widening of the ribbon, which is not attainable due to the confining surface. Instead, the ribbon twists on itself forming two Helical Ribbons (HR), in which the midline draws a helix in space and the saddle-like curvature of the ribbon transitions to isosurfaces with zero mean curvature. The HR can also be described as two interlocking torus knot with invariant $T(1,q)$ where q is related to the ratio of the molecular pitch and the major radius of the tori. Previous works on chiral nematic colloids have characterized these type of knots as linkers for colloidal lattices.[72]

Lastly, we examine the region of systems with $2q_0r_0 > 1$ and $|F_{Ch}|/F_{Splay} > 2$, populated with Blue Phase-like defects. In this regime, one can appreciate the pronounced effects of geometrical frustration on the Helical Blue Phase (HBP). For conditions where confinement is smaller than the unit cell of a BP, disclination lines are interwoven with lingering features of the HR morphology. The defects are evenly spaced but do not always grow radially; instead they follow the helical midline, resulting in sections where the defects form a double helix (drawn in blue), and are encased by two helical ribbons (drawn in green).

Under less severe confinement ($2r_0/a_{BPII} > 2$), a BP unit cell is fully circumscribed by the torus, and replicated throughout the toroidal axis. In such a way, the resulting BP morphologies adopt varying crystallographic orientations, thereby affecting the intensity of the Bragg reflections. In this sense, curvature hinders monocrystallinity but leads to new surface features. For both HBP and BP, the defects are truncated by the curved surface, resulting in a collection of −1/2 defects, spaced by double twist cylinders with +1 topological charge. These structures are most commonly known as half-skyrmions, or merons, and have been observed as dark spots in microscope images. Half-skyrmions are stable and tend to pack in hexagonal lattices; the −1/2 defects form vertices while the +1 defects become the faces of the polygon.

The sequence of transitions, critical values of $|F_{Ch}|/F_{Splay}$ and $2q_0r_0$, and the characteristics of each mesophase are identical to those for cylindrical confinement. This indicates that the role of extrinsic curvature is more nuanced and its effect is not localized. On the other hand, the role of temperature, mediated by the thermal parameter U, reduces the stability region of the DT structure. This becomes apparent when comparing the phase diagrams in Fig. 3a and b, where the slope of $|F_{Ch}|/F_{Splay} = 2$ changes. At lower temperatures, it is more favorable for defects to nucleate, requiring a lower chirality for the double twist to transform into a chiral ribbon structure.

When packed on the surface of a droplet, ''scars'' are formed in the lattice and pairs of 5–7 polygons arise. However, the effect of extrinsic curvature on the packing of half-skyrmions is unclear. We seek to quantify the regularity of the half-skyrmion network with the phenomenological surface parameter Ψ_n,

Open Access Article. Published on 08 June 2023. Downloaded on 4/3/2026 6:47:20 PM.
This article is licensed under a Creative Commons Attribution 3.0 Unported Licence.

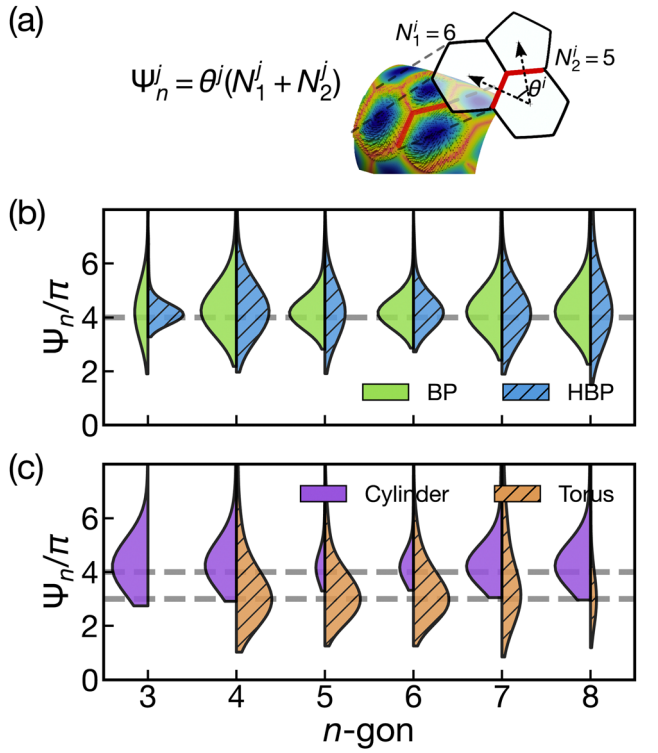

Fig. 4 (a) Schematic representation of the phenomenological surface parameter Ψ_n for a pair of polygon edges i (highlighted in red) with the surface projection from a BP on a curved surface. The coloring of the curved surface corresponds to the orientation of the director field with respect to the surface normal: blue denotes parallel and red corresponds to perpendicular alignment. (b) Probability distribution of Ψ_n for Blue Phase (left, green) and Helical Blue Phase (right, blue) confined in a cylindrical cavity. (c) Probability distribution of Ψ_n for Blue Phases confined in a cylinder (left, purple) and a torus (right, orange).

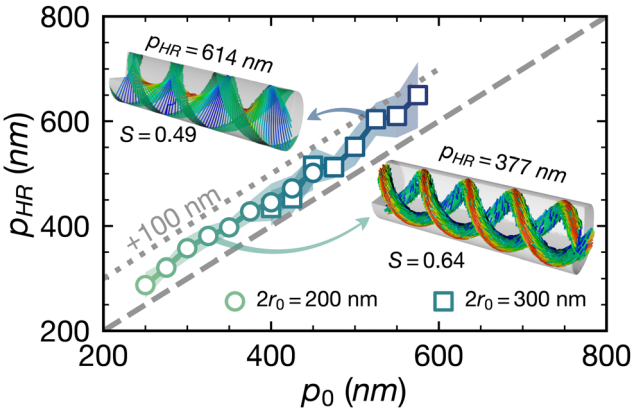

Fig. 5 Pitch of the Helical Ribbon p_{HR} as a function of the molecular pitch in a cylindrical cavity under moderate anchoring conditions ($W = 1 \times 10^{-4}$ J m^{-2}). Error bars are shown by the shaded region. Different markers correspond to the two confinement radii at which this structure is stable. Two morphologies illustrate this structure: in the lower right r_0 = 100 nm and p_0 = 325 nm, and in the upper left r_0 = 150 nm and p_0 = 525 nm. The gray dashed line is the limit for $p_{HR} = p_0$, and the dotted line corresponds to $p_{HR} = p_0 + 100$.

illustrated in Fig. 4a. For each pair of neighboring edges j that belong to an n-gon, $\Psi_n^j = \theta^j(\mathcal{N}_1^j + \mathcal{N}_2^j)$, where $\mathcal{N}_i^j$ are the number of sides of each neighboring polygon. It follows that, for a regular hexagonal network, only Ψ_6 exists, and its probability distribution function is a Dirac delta centered at 4π. The procedure to calculate Ψ_n is as follows. First, the locations where $\boldsymbol{n}\cdot\boldsymbol{\nu} \approx 1$ are extracted and grouped by clusters using the k-means algorithm. The clusters are then compared to the original surface to confirm that the correct polygon centroids have been identified. Using Voronoi and Delaunay triangulation, we successfully identify the edges of each polygon. Additionally, we compute the total topological charge to ensure morphologies are in equilibrium according to the Poincaré–Hopf theorem. We then proceed to calculate Ψ_n for each n-gon found, and we estimate the normalized probability function. This systematic procedure allows us to characterize the differences between BP and HBP morphologies, as well as the role of confinement.

From the violin plot in Fig. 4b, cylindrical confinement broadens the family of polygons expressed on the surface of both BP and HBP. Spherical confinement of a BPII disrupts the regular hexagonal lattice and 5–7 polygon pairs are formed to relieve the stress created by the closed surface. The strict confinement of a cylindrical cavity makes it such that 4–8 pairs of polygons also arise. The probability for Ψ_n in both morphologies is centered around 4π, indicating that all merons are concave polygons. Additionally, the distributions for HBP have a higher variance compared to those of the BP, meaning that the polygons are more irregular in shape. This is a consequence of the helical ribbons interrupting the growth of the defects, and results in the detection of triangular polygons where sections of a ribbon separate merons.

In Fig. 4c, we investigate the effect of extrinsic curvature by comparing BP morphologies in cylindrical and toroidal cavities. As a result of the secondary curvature, the polygon lattice experiences additional strain and the average value of Ψ_n shifts to 3π. This implies that besides the polygons being irregular, each polygon has neighbors with different numbers of sides, leading to an amorphous lattice. Recent experimental and computational work has revealed that these are also characteristics of the Blue Phase III, where the authors suggest it is a fluid composed of skyrmions.[73]

We finish our discussion by exploring the stability of the Helical Ribbon morphology. As explained above, the HR is stable for systems with low natural twist ($2q_0r_0 < 1$) and higher thermal parameter ($U = 2.9$). Furthermore, the chiral elastic energy surpasses the limit of purely cholesteric morphologies ($|F_{Ch}|/F_{Splay} > 2$), with a non-negligible Landau contribution. This indicates that at the center of each ribbon lies a defect core that follows the same helical path. This can be harnessed to drive the assembly of particles into arrays with supramolecular order, since the core of each ribbon will attract particles in order to relieve elastic distortions. Additionally, the helical pattern is imprinted on the surface with tangential orientation of the director, providing an alternative platform for driven assembly of nano or micro particles. Furthermore, the optical

This journal is © The Royal Society of Chemistry 2023

Open Access Article. Published on 08 June 2023. Downloaded on 4/3/2026 6:47:20 PM. This article is licensed under a Creative Commons Attribution 3.0 Unported Licence.

properties of LCs and the precise control over the ribbon pitch can be harnessed to engineer optical guides with spiral paths[74–79]

To further consider potential applications of HR, we also explored how the pitch of the HR (p_{HR}) is connected related to the molecular pitch (p_0)? We performed additional simulations within the stable HR region for cylindrical cavities ($2r_0$ = 200 nm and $2r_0$ = 300 nm) under moderate anchoring conditions ($W = 1 \times 10^{-4}$ J m^{-2}) and U = 2.9. Fig. 5 shows the HR pitch as a function of molecular pitch, including two illustrative HR structures. The pitch was measured from sections throughout the length of each cylinder, and the error bars are represented in the shaded region. There is a linear correlation between both pitches, and the HR pitch is offset by an average of 50 nm from the molecular pitch. The two illustrations represent the helical defect core with p_{HR} = 377 nm, as well as the surface helical pattern with p_{HR} = 614 nm.

4 Conclusions

A theoretical study of chiral liquid crystals confined in cylindrical and toroidal cavities has revealed the existence of new, previously unknown morphologies that arise from the interplay between confining curvature and the inherent twist of the material. These morphologies were generated by relying on a stochastic sampling technique expressed in terms of the five independent components of the order tensor **Q**, which was mapped onto an orthonormal basis set. These morphologies can be classified in terms of three ratios: (i) the natural twist, $2q_0r_0$, which captures the two characteristic dimensions of the system and collapses the free energy onto master curves; (ii) the elastic ratio $|F_{Ch}|/F_{Splay} = 2$, which demarcates the limit above which defects emerge in order to minimize the free energy; (iii) the competition between confinement and the BP cell size $2r_0/a_{BP} = 2$, which determines whether a BP cell can develop or instead adopt helical features. Following a progression of chirality, five morphologies are observed in the underlying phase diagrams when expressed in terms of such ratios: Double Twist, Twisted Ribbon, Helical Ribbon, Helical Blue Phase, and Blue Phase.

An in-depth analysis of the patterns that arise on the surface of the cavities for HBP and BP reveals polygonal lattices, in which −1/2 defects form the vertices and +1 regions form the faces. Our analysis indicates that the HBP is amorphous, mostly due to sections of chiral ribbons that intersect the lattice. In the case of BP, the defects resemble those of BPII, but the geometry interrupts the cubic symmetry that leads to optical activity in narrow ranges. Finally, we discussed how chiral ribbons, and Helical Ribbons, specifically, can serve as a platform for directed assembly. The nature of the helical defect cores makes them a strong candidate for attracting particles, which alleviate elastic stresses, both in the bulk and adsorbed on the surface. The pitch of the ribbon is tunable and it follows a linear relationship with the cavity size and molecular pitch.

Author contributions

J. C. A. P. and V. P. B. performed simulations and calculations. V. P. B., J. C. A. P., and J. P. H. O conducted the analysis of results. V. P. B and J. J. dP wrote the manuscript.

Conflicts of interest

There are no conflicts to declare.

Acknowledgements

The authors wish to thank Chuqiao (Elise) Chen and Dr Pablo Zubieta Rico for valuable discussions. V. P. B. thanks the Fulbright commission in Colombia and Colciencias for support through the PhD student scholarship. This work was supported by the Department of Energy, Basic Energy Sciences, Materials Sciences and Engineering Division, DESC0019762.

References

1 T. Kohyama, D. M. Kroll and G. Gompper, *Phys. Rev. E: Stat., Nonlinear, Soft Matter Phys.*, 2003, **68**, 061905.
2 H. Noguchi, C. Tozzi and M. Arroyo, *Soft Matter*, 2022, **18**(17), 3384–3394.
3 J. Lidmar, L. Mirny and D. R. Nelson, *Phys. Rev. E: Stat., Nonlinear, Soft Matter Phys.*, 2003, **68**, 051910.
4 R. Zandi, D. Reguera, R. F. Bruinsma, W. M. Gelbart and J. Rudnick, *Proc. Natl. Acad. Sci. U. S. A.*, 2004, **101**, 15556–15560.
5 S. Dharmavaram, F. Xie, W. Klug, J. Rudnick and R. Bruinsma, *Phys. Rev. E*, 2017, **062402**, 1–19.
6 A. R. Bausch, M. J. Bowick, A. Cacciuto, A. D. Dinsmore, M. F. Hsu, D. R. Nelson, M. G. Nikolaides, A. Travesset and D. A. Weitz, *Science*, 2003, **299**, 1716–1718.
7 N. Stoop and J. Dunkel, *Soft Matter*, 2018, **14**, 2329–2338.
8 G. Napoli and L. Vergori, *Phys. Rev. E*, 2018, **97**, 52705.
9 P. W. Ellis, D. J. Pearce, Y. W. Chang, G. Goldsztein, L. Giomi and A. Fernandez-Nieves, *Nat. Phys.*, 2017, **14**(1), 85–90.
10 R. Zhang, Y. Zhou, M. Rahimi and J. J. de Pablo, *Nat. Commun.*, 2016, **7**, 13483.
11 M. J. Bowick and L. Giomi, *Adv. Phys.*, 2009, **58**, 139.
12 D. J. Pearce, *Soft Matter*, 2022, **18**, 5082–5088.
13 R. J. Ondris-Crawford, G. P. Crawford, S. Žumer and J. W. Doane, *Phys. Rev. Lett.*, 1993, **70**, 194–198.
14 S. I. Hernández, J. A. Moreno-Razo, A. Ramírez-Hernández, E. Díaz-Herrera, J. P. Hernández-Ortiz and J. J. de Pablo, *Soft Matter*, 2012, **8**, 1443–1450.
15 I. H. Lin, D. S. Miller, P. J. Bertics, C. J. Murphy, J. J. de Pablo and N. L. Abbott, *Science*, 2011, **332**, 1297–1300.
16 D. Miller, X. Wang and N. Abbott, *Chem. Mater.*, 2013, **26**, 496–506.
17 X. Wang, Y. Zhou, V. Palacio-Betancur, Y.-K. Kim, L. Delalande, M. Tsuei, Y. Yang, J. D. Pablo and N. Abbott, *Langmuir*, 2019, **35**, 16312–16323.

Open Access Article. Published on 08 June 2023. Downloaded on 4/3/2026 6:47:20 PM. This article is licensed under a Creative Commons Attribution 3.0 Unported Licence.

18 K. Peddireddy, S. Čopar, K. V. Le, I. Muševič, C. Bahr and V. S. Jampani, *Proc. Natl. Acad. Sci. U. S. A.*, 2021, **118**, e2011174118.
19 J. W. Milnor and D. W. Weaver, *Topology from the Differentiable Viewpoint*, Univ of Virginia Press, 1965.
20 P. W. Oakes, J. Viamontes and J. X. Tang, *Phys. Rev. E: Stat., Nonlinear, Soft Matter Phys.*, 2007, **75**, 1–11.
21 D. Seč, T. Porenta, M. Ravnik and S. Žumer, *Soft Matter*, 2012, **8**, 11982.
22 Y. Zhou, E. Bukusoglu, J. A. Martinez-Gonzalez, M. Rahimi, T. F. Roberts, R. Zhang, X. Wang, N. L. Abbott and J. J. de Pablo, *ACS Nano*, 2016, **10**(7), 6484–6490.
23 H. Yoshida, Y. Tanaka, K. Kawamoto, H. Kubo, T. Tsuda, A. Fujii, S. Kuwabata, H. Kikuchi and M. Ozaki, *Appl. Phys. Express*, 2009, **2**, 121501.
24 Y. Geng, D. Seč, P. L. Almeida, O. D. Lavrentovich, S. Žumer and M. H. Godinho, *Soft Matter*, 2013, **9**, 7928–7933.
25 E. Bukusoglu, X. Wang, Y. Zhou, J. A. Martinez-Gonzalez, M. Rahimi, Q. Wang, J. J. de Pablo and N. L. Abbott, *Soft Matter*, 2016, 8781–8789.
26 Y. Li, J. J. Yan Suen, E. Prince, E. M. Larin, A. Klinkova, H. Thérien-Aubin, S. Zhu, B. Yang, O. D. Lavrentovich and E. Kumacheva, *Nat. Commun.*, 2016, **7**, 12520.
27 V. Palacio-Betancur, J. C. Armas-Pérez, S. Villada-Gil, N. L. Abbott, J. P. Hernández-Ortiz and J. J. de Pablo, *Soft Matter*, 2020, **16**, 870–880.
28 J. A. Martínez-González, Y. Zhou, M. Rahimi, E. Bukusoglu, N. L. Abbott and J. J. de Pablo, *Proc. Natl. Acad. Sci. U. S. A.*, 2015, **112**, 13195–13200.
29 M. Sadati, J. A. Martinez-Gonzalez, Y. Zhou, N. T. Qazvini, K. Kurtenbach, X. Li, E. Bukusoglu, R. Zhang, N. L. Abbott, J. P. Hernandez-Ortiz and J. J. de Pablo, *Sci. Adv.*, 2020, **6**, eaba6728.
30 Y. Yang, V. Palacio-Betancur, X. Wang, J. J. Pablo and N. L. Abbott, *Small*, 2022, **18**, 2105835.
31 V. Vitelli, J. B. Lucks and D. R. Nelson, *Proc. Natl. Acad. Sci. U. S. A.*, 2006, **103**, 12323–12328.
32 T. Lopez-Leon, M. A. Bates and A. Fernandez-Nieves, *Phys. Rev. E: Stat., Nonlinear, Soft Matter Phys.*, 2012, **86**, 1–4.
33 V. Koning, T. Lopez-Leon, A. Fernandez-Nieves and V. Vitelli, *Soft Matter*, 2013, **9**, 4993.
34 A. Darmon, M. Benzaquen, D. Seč, S. Čopar, O. Dauchot and T. Lopez-Leon, *Proc. Natl. Acad. Sci. U. S. A.*, 2016, **113**, 9469–9474.
35 M. Sadati, Y. Zhou, D. Melchert, A. Guo, J. A. Martinez-Gonzalez, T. F. Roberts, R. Zhang and J. J. D. Pablo, *Soft Matter*, 2017, **13**, 7465–7472.
36 A. Javadi, J. Eun and J. Jeong, *Soft Matter*, 2018, **14**, 9005–9011.
37 G. Napoli, O. V. Pylypovskyi, D. D. Sheka and L. Vergori, *Soft Matter*, 2021, **17**, 10322–10333.
38 S. Norouzi, A. Tavera-Vazquez, J. R.-D. Arellano, D. S. Kim, T. Lopez-Leon, J. J. D. Pablo, J. A. Martinez-Gonzalez and M. Sadati, *ACS Nano*, 2022, **16**, 15894–15906.
39 E. Pairam, J. Vallamkondu, V. Koning, B. C. van Zuiden, P. W. Ellis, M. A. Bates, V. Vitelli and A. Fernandez-Nieves, *Proc. Natl. Acad. Sci. U. S. A.*, 2013, **110**, 9295–9300.
40 M. Tasinkevych, M. G. Campbell and I. I. Smalyukh, *Proc. Natl. Acad. Sci. U. S. A.*, 2014, **111**, 16268–16273.
41 D. Jesenek, S. Kralj, R. Rosso and E. G. Virga, *Soft Matter*, 2015, **11**, 2434–2444.
42 L. N. Carenza, G. Gonnella, D. Marenduzzo, G. Negro and E. Orlandini, *Phys. Rev. Lett.*, 2022, **128**, 027801.
43 I. M. Kulić, D. Andrienko and M. Deserno, *Europhys. Lett.*, 2004, **67**, 418–424.
44 J. S. Evans, P. J. Ackerman, D. J. Broer, J. van de Lagemaat and I. I. Smalyukh, *Phys. Rev. E: Stat., Nonlinear, Soft Matter Phys.*, 2013, **87**, 032503.
45 V. Koning, B. C. van Zuiden, R. D. Kamien and V. Vitelli, *Soft Matter*, 2014, **10**, 4192.
46 Y. H. Kim, M.-J. Gim, H.-T. Jung and D. K. Yoon, *RSC Adv.*, 2015, **5**, 19279–19283.
47 R. D. Kamien and T. R. Powers, *Liq. Cryst.*, 1997, **23**, 213–216.
48 J. Jeong, L. Kang, Z. S. Davidson, P. J. Collings, T. C. Lubensky and A. G. Yodh, *Proc. Natl. Acad. Sci. U. S. A.*, 2015, **112**, E1837–E1884.
49 K. Nayani, R. Chang, J. Fu, P. W. Ellis, A. Fernandez-Nieves, J. O. Park and M. Srinivasarao, *Nat. Commun.*, 2015, **6**(1), 1–7.
50 P. W. Ellis, K. Nayani, J. P. McInerney, D. Z. Rocklin, J. O. Park, M. Srinivasarao, E. A. Matsumoto and A. Fernandez-Nieves, *Phys. Rev. Lett.*, 2018, **121**, 247803.
51 J. P. McInerney, P. W. Ellis, D. Z. Rocklin, A. Fernandez-Nieves and E. A. Matsumoto, *Soft Matter*, 2019, **15**, 1210–1214.
52 A. Pedrini and E. G. Virga, *Liq. Cryst.*, 2018, **45**, 2054–2064.
53 C. R. Wand and M. A. Bates, *Phys. Rev. E*, 2019, **100**(5), 052702.
54 E. Dubois-Violette and B. Pansu, *Frustration and Related Topology of Blue Phases*, 1988.
55 F. Castles, S. M. Morris, E. M. Terentjev and H. J. Coles, *Phys. Rev. Lett.*, 2010, **104**, 157801.
56 I. Dierking, W. Blenkhorn, E. Credland, W. Drake, R. Kociuruba, B. Kayser and T. Michael, *Soft Matter*, 2012, **8**, 4355.
57 X. Li, J. A. Martínez-González, K. Park, C. Yu, Y. Zhou, J. J. de Pablo and P. F. Nealey, *ACS Appl. Mater. Interfaces*, 2019, **11**, 9487–9495.
58 X. Li, J. A. Martínez-González, O. Guzmán, X. Ma, K. Park, C. Zhou, Y. Kambe, H. M. Jin, J. A. Dolan, P. F. Nealey and J. J. D. Pablo, *Sci. Adv.*, 2019, **5**, 9112–9141.
59 H. Kikuchi, M. Yokota, Y. Hisakado, H. Yang and T. Kajiyama, *Nat. Mater.*, 2002, **1**, 64–68.
60 E. Kemiklioglu and L. Chy Chien, *Appl. Phys. Express*, 2014, **7**, 091701.
61 I. Gvozdovskyy, *Liq. Cryst.*, 2015, **42**, 1391–1404.
62 M. Sadati, J. A. Martinez-Gonzalez, A. Cohen, S. Norouzi, O. Guzmán and J. J. de Pablo, *ACS Nano*, 2021, **15**, 15972–15981.
63 G. Negro, L. N. Carenza, G. Gonnella, D. Marenduzzo and E. Orlandini, *Soft Matter*, 2023, **19**, 1987–2000.
64 C. Long and J. V. Selinger, *Soft Matter*, 2022, **19**, 519–529.
65 A. Londoño-Hurtado, J. C. Armas-Pérez, J. P. Hernández-Ortiz and J. J. de Pablo, *Soft Matter*, 2015, **11**, 5067–5076.

 This journal is © The Royal Society of Chemistry 2023

Open Access Article. Published on 08 June 2023. Downloaded on 4/3/2026 6:47:20 PM.
This article is licensed under a Creative Commons Attribution 3.0 Unported Licence.

66 J. C. Armas-Pérez, A. Londoño-Hurtado, O. Guzmán, J. P. Hernández-Ortiz and J. J. D. Pablo, *J. Chem. Phys.*, 2015, **143**, 044107.
67 J. C. Armas-Pérez, J. P. Hernández-Ortiz and J. J. de Pablo, *J. Chem. Phys.*, 2015, **143**, 243157.
68 P. Kaiser, W. Wiese and S. Hess, *J. Non-Equilib. Thermodyn.*, 1992, **17**, 153–170.
69 Sandia National Laboratories, CUBIT Geometry and Meshing Toolkit, 2014, **https://cubit.sandia.gov/public/14.1/Cubit-14.1-announcement.html**.
70 B. S. Kirk, J. W. Peterson, R. H. Stogner and G. F. Carey, *Eng. Comput.*, 2006, **22**, 237–254.
71 M. Sadati, A. I. Apik, J. C. Armas-Pérez, J. A. Martínez-González, J. P. Hernández-Ortiz, N. L. Abbott and J. J. de Pablo, *Adv. Funct. Mater.*, 2015, **25**, 6050–6060.
72 U. Tkalec, M. Ravnik, S. Čopar, S. Žumer and I. Muševič, *Science*, 2011, **333**, 62–65.
73 J. Pišljar, S. Ghosh, S. Turlapati, N. Rao, M. Škarabot, A. Mertelj, A. Petelin, A. Nych, M. Marinčič, A. Pusovnik, M. Ravnik and I. Muševič, *Phys. Rev. X*, 2022, **12**(1), 011003.
74 S. Slussarenko, A. Alberucci, C. P. Jisha, B. Piccirillo, E. Santamato, G. Assanto and L. Marrucci, *Nat. Photonics*, 2016, **10**(9), 571–575.
75 M. Ravnik and J. Pišljar, *Opt. Express*, 2018, **26**(20), 26327–26338.
76 G. Poy, A. J. Hess, A. J. Seracuse, M. Paul, S. Žumer and I. I. Smalyukh, *Nat. Photonics*, 2022, **16**, 454–461.
77 M. G. Clerc, G. González-Cortés and S. Echeverría-Alar, *Phys. Rev. Res.*, 2022, **4**, L022021.
78 H. Abbaszadeh, M. Fruchart, W. van Saarloos and V. Vitelli, *Proc. Natl. Acad. Sci. U. S. A.*, 2021, **118**, e2020525118.
79 S. Echeverría-Alar, M. G. Clerc and I. Bordeu, *Proc. Natl. Acad. Sci. U. S. A.*, 2023, **120**, e2221000120.